Application of linear frequency modulated laser ultrasonic radar in reflective thickness and defect non-destructive testing

Huiting Huan[a,b], Andreas Mandelis[b,*], Lixian Liu[b], Bahman Lashkari[b], Alexander Melnikov[b]

[a] School of Mechano-Electronic Engineering, Xidian University, Xi'an, 710071, China
[b] Center for Advanced Diffusion-Wave and Photoacoustic Technologies (CADIPT), Department of Mechanical and Industrial Engineering, University of Toronto, Toronto, ON, M5S 3G8, Canada

ABSTRACT

Radar technology plays an important role in modern aviation and navigation. Radar systems use pulse-compression and match-filtering to detect large moving objects in the sky or in water, or small defects hidden inside industrial components, the object of this paper. We introduce a nondestructive testing (NDT) modality based on frequency-domain laser ultrasound (FDLU) by means of implementing radar principles: Linear-frequency-modulated (LFM chirp) excitation CW laser-beam intensity to perform, ultrasonic signal cross-correlation with the reference signal using pulse-compression and match-filtering, leading to reconstruction of time-domain sequences through inverse Fourier transformation at acceptable signal-to-noise ratios. Theoretically, the laser ultrasound radar (LUR) signal was modelled with both one- and three-dimensional thermoelastic equations, a combination of which was used to simultaneously predict the correct location and relative amplitude of experimental targets with relatively simple mathematical expressions that could not be used either in the 1-D (too simplistic) or in the 3-D (too complicated) approach alone. This methodology was further used to detect buried defects inside a metal alloy. The results demonstrated that the LUR system is capable of determining the thickness of the alloy material and quantitatively estimate the subsurface depth of defects in a signal generation process akin to echolocation.

1. Introduction

In radar and sonar systems, a pulse compression technique is used as an alternative to obtain generating a single high-peak-power and short-duration electromagnetic/ultrasonic (US) pulse to obtain time-domain signals with enhanced signal-to-noise ratio (SNR) by sending a relatively long, wide-bandwidth, coded pulse and compressing the received pulse into a much narrower response which depends of the time-bandwidth product [1,2]. Such a signal generation arrangement when implemented with laser systems has the advantage of requiring a significantly smaller laser source and simplified instrumentation system at the expense of more sophisticated signal processing methods. In the field of photoacoustic non-destructive testing (NDT), laser ultrasound mainly operates in the time-domain and relies heavily on high performance solid-state pulsed lasers [3–5]. Nevertheless, the photo-thermo-elastic conversion coefficient is extremely small ($\sim 10^{-7}$) if operating below the destructive laser intensity threshold, and the relatively low SNR is a severe problem especially with industrial alloy samples [6]. To improve the situation, instead of resorting to high intensity short-pulsewidth laser sources and wide-bandwidth optical detectors, a useful testing schematic is the laser ultrasound radar (LUR), also known as the photoacoustic radar (PAR), which adopts cost effective, small footprint CW laser diode sources and narrowband piezoelectric transducers. Such a configuration applied to biomedical photoacoustics has proven to be able to obtain an SNR [7–9] comparable to pulse excitation time-domain laser ultrasound [10,11]. In our earlier work [7–12] we focused mainly on biomedical tissues in which the laser beam can travel a certain distance and generate back-scattered acoustic waves by means of the photo-thermo-elastic effect. The most important information is obtained from the cross-correlation peak itself and thus no reflected ultrasound peak (echolocation principle) is involved. For opaque metallic materials however, light absorption only takes place at the surface with no light energy penetrating into the sample. In this case laser ultrasound can be used to evaluate material parameters and subsurface defects by acoustic echo analysis. In this work, a systematic investigation of LUR echolocation implemented on metal alloy samples is presented. We show that the LUR can determine variations in sample thickness and the depth of defects.

---

* Corresponding author.
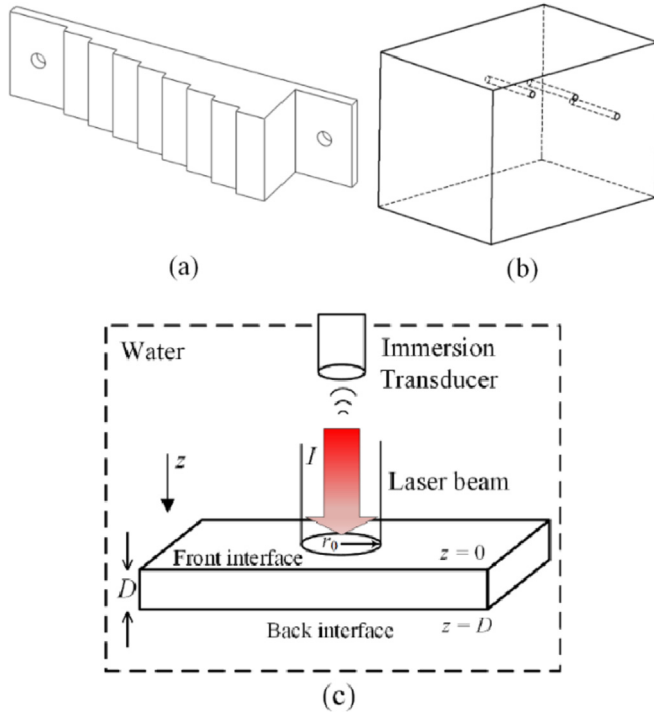   E-mail address: mandelis@mie.utoronto.ca (A. Mandelis).

Fig. 1. (a) Aluminum step sample used for thickness detection; **(b)** stainless block with 3 buried holes; **(c)** schematic for the theoretical model.

2. Experimental

The LUR configuration used in this work is that of a typical frequency-domain photoacoustic system. A 3-W (RMS power) diode laser was linear-frequency-modulated (LFM) using a chirp from 300 kHz to 2 MHz with a $\sim$ 4-mm beam size in diameter at oblique incidence. Two samples were used in this test as shown in Fig. 1(a) and (b). An aluminum alloy sample with steps of different thicknesses was used to verify the capability of the LUR system to measure thickness. Furthermore, a piece of stainless steel with artificial horizontal holes at various depths was machined to test the possibility of defect detection by the reflected laser-generated ultrasound. The laser induced chirped thermoelastic waves propagated in a water couplant and were detected by an immersion ultrasound transducer (Panametrics® v314, nominal frequency 1 MHz) placed right above the laser spot. The system was controlled by a computer with National Instruments® signal generation and a data acquisition card which was also responsible for match-filtering of the received acoustic signal as described in Ref. [8].

3. Theoretical background

The modulated incident laser power density was low enough to ensure the thermoelastic (rather than ablative) modality by which the ultrasonic wave was generated as a result of thermal expansion upon surface absorption without damaging the sample surface. In such a situation, the laser ultrasound signal can be analytically described with a comprehensive photo-thermo-elastic theory with either a 1D or a semi-infinite 3D approximation. Both models are adopted in the following analysis and compared with experimental data to develop an optimized composite theory. The reason for considering a 1-D laser thermoelastic model mixed in with the more detailed 3-D model is that the combined approach is the least complicated way of modeling interface reflection signals in a finite thickness elastic material. Furthermore, based on the features of the tested industrial samples, a couple of basic assumptions were adopted: a) Purely surface light absorption. Alloys are conductors with large free electron densities so that optical absorption, reflection

and scattering all occur within a very shallow layer (< 100 Å) from the surface [13]; b) Infinite lateral dimensions. The experimental samples had much larger lateral dimensions than their thickness. Lateral reflections were thus ignored in the 3-D model.

3.1. One-dimensional laser-chirp-induced thermoelasticity

The physical model is shown in Fig. 1(c) and incorporates the infinite lateral extent of the solid. Laser ultrasound generation is associated with uniform heating and longitudinal stress waves only [14,15]. The thermoelastic equations for frequency-domain independent variables temperature T, longitudinal stress s and vertical displacement component w, are respectively:

$$-\kappa \partial^2 T/\partial z^2 + i\omega\rho CT = \beta I_f(\omega)\delta(z) \tag{1a}$$

$$\partial s/\partial z - (3\lambda + 2\mu)\alpha_e T(z, \omega) + \rho\omega^2 w = 0 \tag{1b}$$

where κ, α_e, ρ, C are the thermal conductivity, the linear thermal expansion coefficient, the density and the specific heat capacity of the solid, respectively; λ and μ are its first and second Lamé constants. $\omega = 2\pi f$ is angular frequency. Solving this problem analytically requires the linear elastic stress-strain relation, viz. $s = (\lambda + 2\mu)\partial w/\partial z$. The heating source term I_f is the Fourier spectrum of the chirp modulated laser intensity:

$$I_f(\omega) = \int_0^{+\infty} I(t)\exp(i\omega t)dt \tag{2a}$$

where

$$I(t) = I_0 \cos(\omega_c t + \pi B_c T_c^{-1} t^2), -T_c/2 < t < T_c/2 \tag{2b}$$

The central angular frequency ω_c, bandwidth B_c and chirp duration T_c etc. are defined in Ref. [8]. For a finite thickness sample, the harmonic solutions for the displacement and water-coupled outgoing acoustic pressure are:

$$p(z, \omega) = A_1 \exp(ik_0 z) \tag{3a}$$

$$w(z, \omega) = B_1 \exp(-ik_l z) + B_2 \exp(ik_l z) + B_3 \exp(-\alpha z) \tag{3b}$$

$$B_3 = -\frac{(3\lambda + 2\mu)\beta\alpha_e I_f(\omega)}{(i\omega\rho C + \kappa k_l^2)(\lambda + 2\mu)} \tag{3c}$$

$k_0 = \omega/c_0$ and $k_l = \omega/c_l$ are angular wavevectors in water and sample, respectively. It should be noted that in Eq. (3a) the pressure wave is assumed to be strictly forward travelling and does not include a reflection term introduced by the transducer surface which normally should be considered in a harmonic modulation laser ultrasound scheme [16]. By applying match-filtering and reconstructing the signal in time-domain, the first back-propagated LUR signal can be easily separated out and the sample-transducer inter-reflections can be completely eliminated. Also, the sample becomes strictly semi-infinite with respect to thermal waves within the ultrasonic frequency range and the adiabatic boundary condition is reasonable to use on the front surface [16]. The three unknowns (A_1, B_1, B_2) require three boundary conditions on both sides of the interface (as illustrated in Fig. 1(c)). At $z = 0$, both pressure and velocity are continuous, which yields:

$$p(0, \omega) = s(0, \omega) \text{ or } A_1 = c_l^2\rho(-ik_l B_1 + ik_l B_2 - \alpha B_3) \tag{4a}$$

$$i\omega w(0, \omega) = Z_0^{-1}p(0, \omega) \text{ or } A_1 = i\omega Z_0(B_1 + B_2 + B_3) \tag{4b}$$

$Z_0 = \rho_0 c_0$ is the acoustic impedance of water. At $z = D$, total reflection is assumed which is equivalent to a motion-free surface, viz.

$$\partial w/\partial z|_{z=D} = 0 \text{ or } -ik_l e^{-ik_l D}B_1 + ik_l e^{ik_l D}B_2 = 0 \tag{4c}$$

The parameter of interest representing the pressure wave can now be solved for:

$$p(z, \omega) = \frac{Z_0 \left[i\omega \left(1 - e^{-2ik_l D} \right) - c_l (i\omega\rho C/\kappa)^{1/2} \left(1 + e^{-2ik_l D} \right) \right]}{\left(1 - e^{-2ik_l D} \right) - \gamma_{0s} \left(1 + e^{-2ik_l D} \right)} B_3 \exp(ik_0 z)$$

(5)

where $\gamma_{0s} = Z_0/\rho c_l$ is the acoustic impedance ratio between water and solid.

3.2. Three-dimensional azimuthally symmetric thermoelasticity

The reason for considering the 3-D thermoelastic theory is the inability of the 1-D theory to explain horizontal displacement or lateral radiation of elastic waves, thus resulting in no dissipation of ultrasonic energy. To depict elastic waves in a laterally unbounded, finitely thick solid, it is convenient to use the displacement potential instead of displacement field which can be mathematically derived as:

$$\mathbf{u} = (u, v, w) = \nabla\phi + \nabla \times \boldsymbol{\psi}$$

(6)

Under azimuthally symmetric conditions, the vector potential $\boldsymbol{\psi}$ consists of only one component along the azimuthal direction ψ in cylindrical coordinates. The temperature distribution is described by the thermal-wave equation while the pressure wave, scalar and vector potential all satisfy the wave equations [16,17]:

$$-\kappa r^{-1}\partial(r\partial T/\partial r)/\partial r - \kappa\partial^2 T/\partial z^2 + i\omega\rho C T = \beta I'_f(r, \omega)\delta(z)$$

(7a)

$$r^{-1}\partial(r\partial p/\partial r)/\partial r + \partial^2 p/\partial z^2 + k_0^2 p = 0$$

(7b)

$$r^{-1}\partial(r\partial\phi/\partial r)/\partial r + \partial^2\phi/\partial z^2 + k_l^2\phi = (3\lambda + 2\mu)(\lambda + 2\mu)^{-1}\beta T(r, z, t)$$

(7c)

$$r^{-1}\partial(r\partial\psi/\partial r)/\partial r - r^{-2}\psi + \partial^2\psi/\partial z^2 + k_s^2\psi = 0$$

(7d)

$$I'_f(r, \omega) = \int_0^{+\infty} I'(r, t)\exp(i\omega t)dt, \ I'(r, t) = I(t)(2\pi)^{-1}\exp(-r^2/r_0^2)$$

(7e)

with similar boundary conditions to those of Eq. (4). $k_s = \omega/c_s$ is the shear angular wavenumber corresponding to the propagation wavevector. The source term $I'_f(r, \omega)$ becomes a spatial-coordinate term with respect to radial coordinate r. Introducing the Hankel transform with respect to the radial coordinate r for the four variables T, p, φ and ψ with Bessel functions of the first kind of order 0, 0, 0 and 1, respectively, after some mathematical manipulation the analytical solution for the pressure wave in the Hankel domain can be derived as:

$$\hat{p}(\zeta, z, \omega) = \mu[(\zeta^2 M_1 - 2\zeta\sigma_s)C_1 + (\gamma^2 N_2 + 2\zeta\sigma_s)C_2 + \gamma^2\hat{B}_3]\exp(-\sigma_p z)$$

(8a)

where,

$$C_1 = [(\gamma^2 - 2\zeta\sigma_l M_2)C_2 - 2\zeta\alpha\hat{B}_3](2\zeta\sigma_l N_1 - \gamma^2)^{-1}$$

(8b)

$$C_2 = \left(\frac{2\zeta\alpha}{2\zeta\sigma_l N_1 - \gamma^2} - \frac{\gamma^2 + \rho_0\omega^2\alpha/(\sigma_p\mu)}{\gamma^2 M_1 - 2\zeta\sigma_s + \rho_0\omega^2/(\sigma_p\mu)(\sigma_l N_1 - \zeta)} \right)\hat{B}_3$$

$$\cdot \left[\frac{\gamma^2 - 2\zeta\sigma_l M_2}{2\zeta\sigma_l N_1 - \gamma^2} + \frac{\gamma^2 N_2 + 2\zeta\sigma_s + \rho_0\omega^2/(\sigma_p\mu)(\sigma_l M_2 - \zeta)}{\gamma^2 M_1 - 2\zeta\sigma_s + \rho_0\omega^2/(\sigma_p\mu)(\sigma_l N_1 - \zeta)} \right]^{-1}$$

(8c)

$$\left. \begin{array}{l} M_1 = \gamma^2 e^{\sigma_s D}(2\zeta\sigma_l)^{-1}\sinh(\sigma_l D) + 2\zeta\sigma_s e^{-\sigma_s D}\gamma^{-2}\cosh(\sigma_l D) \\ N_1 = \gamma^2 e^{\sigma_s D}(2\zeta\sigma_l)^{-1}\cosh(\sigma_l D) + 2\zeta\sigma_s e^{-\sigma_s D}\gamma^{-2}\sinh(\sigma_l D) \\ M_2 = \gamma^2 e^{\sigma_s D}(2\zeta\sigma_l)^{-1}\cosh(\sigma_l D) - 2\zeta\sigma_s e^{\sigma_s D}\gamma^{-2}\sinh(\sigma_l D) \\ N_2 = \gamma^2 e^{-\sigma_s D}(2\zeta\sigma_l)^{-1}\sinh(\sigma_l D) - 2\zeta\sigma_s e^{\sigma_s D}\gamma^{-2}\cosh(\sigma_l D) \end{array} \right\}$$

(8d)

$$\hat{B}_3(\omega, \zeta) = \frac{\beta\alpha_e I_f(\omega)(3\lambda + 2\mu)\exp(-r_0^2\zeta^2/4)}{2\pi\alpha(i\omega\rho C + \kappa k_l^2)(\lambda + 2\mu)}$$

$$\alpha^2 = \zeta^2 + i\omega\rho C/\kappa, \ \sigma_p^2 = \zeta^2 - k_0^2, \ \sigma_{l,s}^2 = \zeta^2 - k_{l,s}^2, \ \gamma^2 = 2\zeta^2 - k_s^2,$$

(8e)

The expression for $\hat{B}_3$ includes the Gaussian beam term in contrast with the uniform illumination 1-D Eq. (3c). In Eq. (8) ζ is the spatial frequency variable in the Hankel domain with respect to radial coordinate r. Inverse Hankel transformation is required as the last step to restore the pressure wave field in the spatial domain which includes an improper integral

$$p(r, z; \omega) = \int_0^{+\infty} \hat{p}(\zeta, z; \omega)J_0(\zeta r)\zeta d\zeta$$

(9)

Before performing the integration numerically, it is necessary to discuss the integrand in Eq. (9) which has several real-axis singularities and could possibly hinder the integration. The first singularity appears to be located at $\zeta = 0$, however, this point is not singular because the following limit can be obtained:

$$\lim_{\zeta \to 0} \hat{p}(\zeta, z, \omega) = -k_s^2\hat{B}_3(\omega, 0)\exp(-ik_p z)$$

(10a)

For the case $\zeta \to k_l$, the limits of M_1, N_2 exist and are infinite for M_2, N_1 in Eq. (8d), but they do not represent singularities because the following combinations remove the infinities:

$$\lim_{\zeta \to k_l}[\sigma_l M_2] = \exp(-2\sqrt{k_l^2 - k_s^2}D)\cdot\lim_{\zeta \to k_l}[\sigma_l N_1]$$

$$= (2k_l^2 - k_s^2)\exp(-\sqrt{k_l^2 - k_s^2}D)/2k_l$$

(10b)

$$\lim_{\zeta \to k_l}[\sigma_l(M_1 M_2 - N_1 N_2)] = 2\sqrt{k_l^2 - k_s^2}\cosh(2\sqrt{k_l^2 - k_s^2}D)$$

(10c)

The foregoing two limits further result in a removable discontinuity at $\zeta = k_l$. The third case is $\zeta \to k_s/\sqrt{2}$ which results in $\gamma = 0$ and the limit

$$\lim_{\zeta \to k_s/\sqrt{2}} \hat{p}(\zeta, z, \omega) = -\frac{k_s(k_s^2/2 + i\omega\rho C/\kappa)}{\sqrt{k_s^2 - 2k_l^2}} \frac{\exp(-\sqrt{k_s^2/2 - k_p^2}z)}{\tanh(\sqrt{k_s^2/2 - k_l^2})}\hat{B}_3(\omega, k_s$$

$$/\sqrt{2})$$

(10d)

exists, thereby not representing a singularity but only another removable discontinuity. Similarly, it is easy to prove $\zeta = k_p$ is also nonsingular. The other singularities are all complex numbers and will not be included in the integration. It is also noted that the integration cannot be performed in the complex plane with the application of the residue theorem since a suitable enclosed contour is absent. Following these considerations, the improper integration was performed numerically using a Gauss-Kronrod quadrature [18].

3.3. The match-filtering algorithm

The basic principle of match-filtering is the cross-correlation between detected signal and reference/excitation that will generate a sequence of time-delayed echoes. In the frequency-domain such operation can be simplified as the product of the received detector signal and the complex conjugate of the modulation signal:

$$S(t) = \int_0^{+\infty} s_r(\tau)I(t + \tau)d\tau = \mathcal{F}^{-1}\{p(-L, \omega)\cdot H_{tr}(\omega)\cdot I_f^*(\omega)\}$$

(11)

Here, $s_r(t)$ is the output signal of the transducer given by the convolution of the pressure wave $p(t)$ and the transducer impulse response function $h_{tr}(t)$. From the expression of the pressure wave field, the source term is included in B_3 or $\hat{B}_3$ and the cross-correlation simply becomes an auto-correlation with the identity $I_f(\omega)\cdot I_f^*(\omega) = \|I_f(\omega)\|^2$ involved in Eq. (11). The additional information required in Eq. (9) is the system transfer function. An insightful theoretical model of the transducer and the photoacoustic signal output can be found elsewhere [8,19,20]. In this paper, the relative FWHM of the LUR signal peaks is not a factor of interest and this term is omitted.

4. Results and discussion

4.1. Thickness measurements

The multi-step sample shown in Fig. 1(a) was used for thickness measurement experiments. Since it had much larger lateral dimensions than its thickness, any signals resulting from reflections at the lateral sides were not superposed on the thickness echo and thus could be
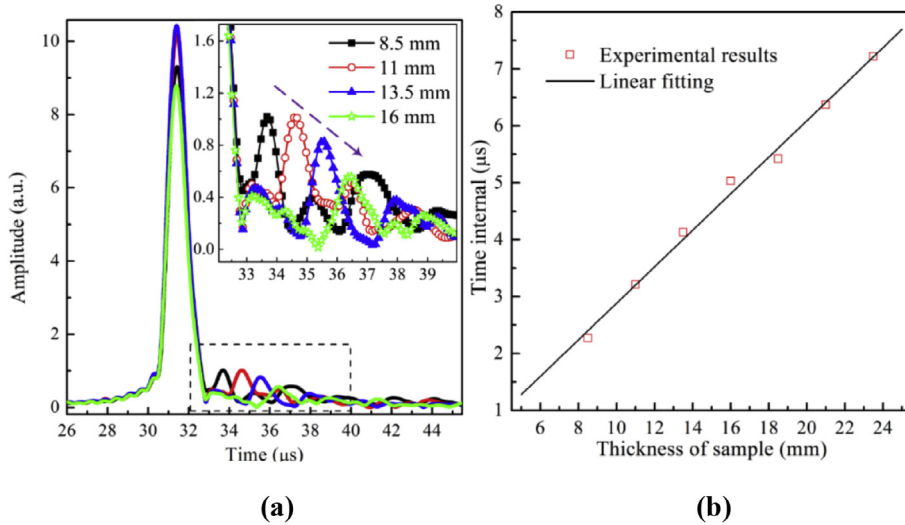
Fig. 2. The LUR thickness measurements. **(a)** LUR time-domain signal (the inset is a magnification of the evolution of the back surface echoes (BSEs) of different sample thicknesses); **(b)** Time-thickness relation using the interval between the direct response (DR) and BSEs.

easily truncated out in the time-domain after cross-correlation. The detected acoustic signals were match-filtered with respect to the laser modulation reference signal. The group of signals from different thicknesses is shown in Fig. 2(a). The time resolved LUR signal exhibits distinctive peaks as a result of pulse compression. For all samples the strongest peak is located at ~31 μs and is the laser-induced ultrasonic response propagating directly to the transducer, henceforth named "the direct response" (DR) peak. The subsequent small peaks (magnified in the inset) are the round-trip reflection signals and represent the back surface echoes (BSE). The BSEs evolve gradually with increasing thickness from higher, narrower, and earlier-arriving to lower, wider, and more delayed responses. Such features can be easily explained with reflection, scattering and lateral energy transport of elastic waves inside the solid medium. The interval between DR and BSE indicates the elastic wave propagation velocity, as shown in Fig. 2(b). The calculated velocity was 6232 (±226) m/s which is the longitudinal wave velocity of the aluminum alloy (typical values vary from 6149 to 6412 m/s depending on different manufactures and products [21,22]). The uncertainty may come from two factors, i.e. the inaccuracy of thickness measurement and the time interval error between the two peaks.

To match the experimental results to theory, the foregoing theoretical analysis was used in a numerical computation. The cross-correlation operation was performed as a multiplication in frequency-domain and converted to time-domain by a fast Fourier transform (FFT). The reference LFM signal I_t in Eq. (2b) has a power spectrum shown in Fig. 3(a). The ripples are the natural characteristics of the LFM FFT. Fig. 3(b) shows the spectra of the recorded pressure wave with both 1-D and 3-D models. Fig. 3(c) plots the cross correlations. The transducer was placed 50 mm above the laser spot, and the corresponding DR location was about ~31.5 μs. Sample thickness used in the simulation was 8.5 mm and the first BSE occurred ~2.8 μs behind the DR. By applying 1-D theory, the interreflections between the front and back surfaces of the material are clearly shown in terms of echo peaks. Multiple BSEs exhibit a gradually decreasing pattern of large reflection peaks commensurate with the DR peak. This is inconsistent with the experimental results, Fig. 2(a) which show a dominant DR peak much higher than all BSEs. By contrast, the 3-D model gives the right location and amplitude level of the DR peak as shown, but since the directivity of the longitudinal wave induced by laser surface heating involves strong sidelobes in the acoustic radiation pattern [6,17], longitudinal wave energy is dissipated rapidly and the BSEs are too small and buried in cross-correlation-induced ripples, thereby becoming invisible. The discrepancy between the finite lateral dimension of the experimental
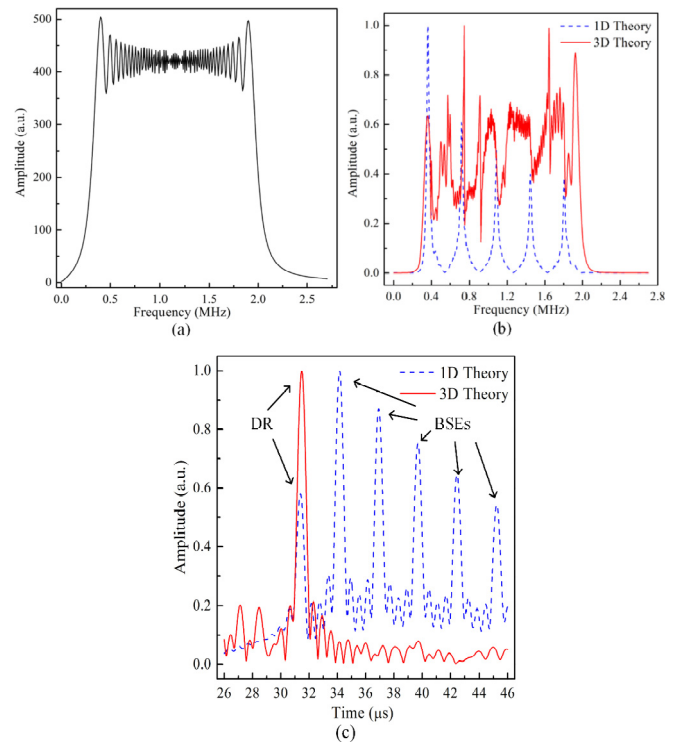

Fig. 3. **(a)** power spectrum of laser chirp ((#1–7)300 kHz–2 MHz); **(b)** Calculated normalized acoustic power spectra using the 1-D and 3-D theories; **(c)** Match-filtered LUR signals using the 1-D and 3-D theories.

sample and the assumption made in 3D model could also be responsible for the BSE invisibility. To resolve this unsatisfactory situation, an empirically combined physical model was used to predict a) the amplitude (3-D approach) and b) the location (1-D approach) of the BSEs. An *ad-hoc* linear combination of the two models yields:

$$p_t(0, z; t) = \int_{-\infty}^{+\infty} [ap(z, \omega) + b\int_0^{+\infty} \hat{p}(\zeta, z; \omega)\zeta d\zeta] \exp(i\omega t)d\omega \qquad (12)$$

where a and b are real adjustable parameters. The 1-D and 3-D pressure terms originate in Eqs. (5) and (8a), respectively. Fig. 4 shows the comparison between the experimental data and the combined theory predictions. Regarding the DR, both 3-D and combined theory can locate them with excellent accuracy. In addition, the combined theory
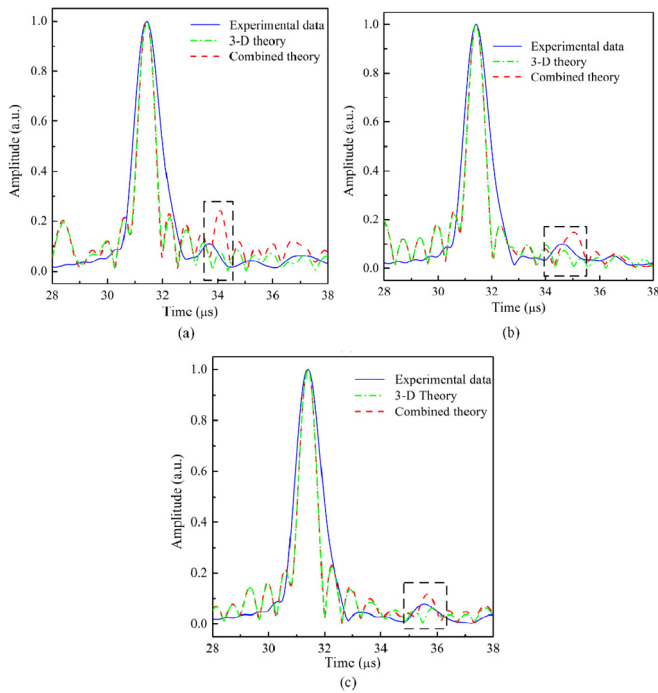
Fig. 4. Comparison between LUR theoretical predictions and experimental results with various sample thicknesses (the dashed windows indicate the BSE of interest, $a = 1$ and $b = 1.5$ in Eq. (11)): (a) 8.5 mm, (b) 11 mm, (c) 13.5 mm. The narrower theoretical DR and BSE peak FWHMs are due to omission of the transducer transfer function.

features a gradual change of BSE location and peak width with thickness variation which cannot be readily identified with the 3-D theory due to the presence of strong sidelobes. The narrower theoretical DR and BSE peak FWHMs are due to the omission of the transducer transfer function. Since the elastic properties of the tested sample cannot be precisely known, there is a slight difference in BSE location between theory and experiment. Nonetheless, the combined theory can successfully interpret the pattern of BSE with increasing thickness.

Conventional time-of-flight (TOF) thickness measurements with the photoacoustic approach usually adopt a pulsed laser as the excitation source. Specific delay-time control systems and time-frequency domain analysis are required to ensure the detectability and SNR of TOF signals [23,24]. However, the foregoing results show that by simply using a modulated CW laser diode source, the sample thickness can be remotely measured from the time-delayed photoacoustic signal by match-filtering which sufficiently decreases the optical power requirements and enhances flexibility.

4.2. Defect detection

The next experimental investigation with the LUR system was to locate buried defects by using the foregoing US reflection analysis. Three horizontal holes (diameter: 2 mm) were machined 5 mm, 10 mm, and 20 mm below the surface of the stainless steel block as shown in Fig. 1(b). A B-scan schematic is shown in Fig. 5(a). The horizontally inclined subsurface hole ("defect") located 5 mm deep produced the curves shown as an example in Fig. 5(b). Care was taken for the relative distance between the ultrasonic transducer and the laser beam to remain fixed during the scanning process. The number of scan steps was quite limited, so we plotted the group of curves from locations with all considered "defects" with a single time coordinate shown in Fig. 5(b). Since the sample thickness was much larger than the defect depth, the BSEs were not recorded or considered in the ensuing data analysis. The combined theory successfully predicted the changed signal pattern near the location of the echo produced by each defect. Again, due to the
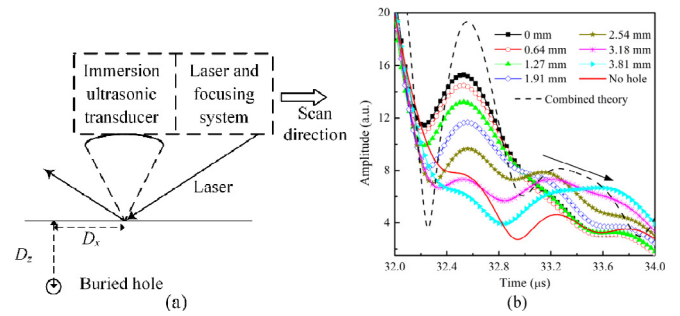

Fig. 5. (a) Schematic of LUR B-scan for subsurface defect inspection applications; **(b)** Defect echoes (DEs) for a hole $D_z = 5$ mm deep at delay times corresponding to scanned horizontal distance D_x.

omission of the transducer transfer function and the uncertainty of the actual elastic behavior of the material, the theoretical FWHM is narrower than the experimental FWHM. The defect echoes (DEs) exhibit a decreasing magnitude and more time-delayed trends with continuously increasing distance from the hole as the system scans away from the vertical position ($D_x = 0$) directly above the hole, as expected. The curve marked "No hole" was used as a reference obtained by scanning an area far away from the holes.

In order to quantify the response pattern, these DEs must be normalized with respect to an "intact" material reference without subsurface holes. The significance of this procedure is two-fold: to eliminate the spurious ripples resulting from internal transducer reflections and the sidelobes due to match-filtering, and to exclude the influence of different surface conditions at various scanning locations. An ideal reference peak for these curves would be the DR which should be regarded as the same at all lateral locations. Taking a no-hole DR as the reference, the seven curves in Fig. 5(b) were first normalized to have their DR peaks at the same height, then followed by a normalization (division) of all the other curves with the intact curves so as to reveal the echoes from the defect. The example of the 5-mm deep hole is considered again in Fig. 6. A conspicuous right shift of the peaks reveals the fact that the buried defect gradually moves away from the scanned laser beam location. The propagation of the elastic wave from the hole to the scanning system's transducer focal point by reflection can be
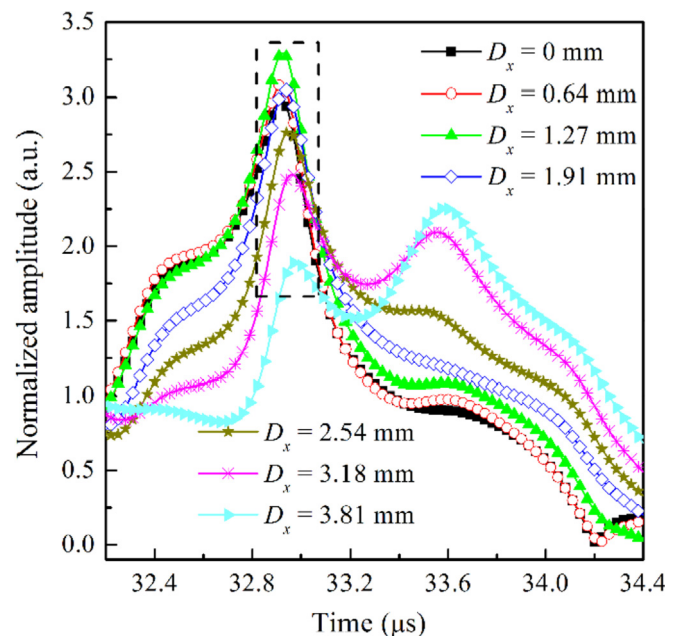

Fig. 6. Normalized LUR signal with obvious BSEs trends due to a subsurface hole at $D_z = 5$ mm.

Table 1
Subsurface defect location detection by the LUR technique showing actual and estimated depths.

Defects ID	Real depth	LUR Estimated depth
Hole 1	5 mm	5.13 ± 0.47 mm
Hole 2	10 mm	9.59 ± 0.04 mm
Hole 3	20 mm	19.86 ± 0.07 mm

estimated simply from the Pythagorean theorem as:

$$D_z \approx \sqrt{(c_l \Delta t/2)^2 - D_x^2} \tag{13}$$

where c_l is the longitudinal wave speed in the stainless steel sample and Δt is the time interval between DR and DEs. It should be noted that this estimation does not consider the diameter of the hole because its dimension is slightly smaller than the elastic wavelength in the sweeping frequency range. The echo is regarded as generated from the center of the hole instead of its surface. Adopting $c_l = 5865$ m/s as the elastic wave speed for the stainless steel sample [25] we obtained the estimated depth of the three holes as shown in Table 1. The hole depths are estimated by Eq. (13) and the uncertainty is determined from the fitting error. The result of the 5 mm hole defect shows the largest uncertainty. This is because the error of time interval estimation and the impact of cross-correlation-induced ripple lead to a more severe variance for shallower defects. It is concluded that the LUR technique proves to be considerably accurate in locating subsurface hole defects down to 20 mm. From our experimental data we believe that this is not an upper depth limit for subsurface hole detection.

The foregoing experimental tests were based on an immersion transducer which still does not provide a rigorous non-contact measurement. For practical field applications, a re-designed air-coupled ultrasonic transducer or a fully optical vibrometer can render the system fully non-contacting. Use of higher frequency ranges with US wavelengths smaller than defect dimensions will also improve spatial resolution and detectability at the expense of depth penetration.

5. Conclusions

This research has developed a novel laser ultrasound radar system to perform thickness measurements and NDT analysis of buried defects. The LUR system avoids using a pulsed laser and a contact ultrasonic transducer, and is able to operate in a non-contact mode. The diode laser was chirp modulated with a LFM from hundreds of kHz to 2 MHz. Pulse compression, match-filtering and cross-correlation of the received chirp signals transformed the system response into the time-domain. In the application of thickness measurements, back surface echoes were detected after the DR peak and were successfully interpreted and predicted by a combination of 1-D and 3-D thermoelastic theory. The LUR echolocation scheme was also used for the detection of hidden defects. With the calculated (or known) longitudinal wave velocity of the sample, the depths of defects were estimated with excellent accuracy.

Acknowledgements

References

[1] Cohen MN. Pulse compression in radar systems. In: Eaves JL, Reedy EK, editors. Principles of modern radar. Boston: Springer; 1987. p. 465–501.

[2] Farnett EC, Stevens GH. Pulse compression radar. Radar handbook. New York: McGraw-Hill; 1990. chap.10.

[3] Dewhurst RJ, Hutchins DA, Palmer SB, Scruby CB. Quantitative measurements of laser generated acoustic waveforms. J Appl Phys 1982;53:4064.

[4] Hutchins DA. Mechanisms of pulsed photoacoustic generation. Can J Phys 1986;64:1247–64.

[5] Arnold W, Betz B, Hoffmann B. Efficient generation of surface acoustic waves by thermoelasticity. Appl Phys Lett 1985;47:672.

[6] Scruby B, Drain LE. Laser ultrasonics techniques and applications. Bristol: Adam Hilger; 1990. Chap.2.

[7] Lashkari B, Mandelis A. Photoacoustic radar imaging signal-to-noise ratio, contrast, and resolution enhancement using nonlinear chirp modulation. Opt Lett 2010;35:1623–5.

[8] Lashkari B, Mandelis A. Linear frequency modulation photoacoustic radar: optimal bandwidth and signal-to-noise ratio for frequency-domain imaging of turbid media. J Acoust Soc Am 2011;130:1313–24.

[9] Telenkov S, Mandelis A. Signal-to-noise analysis of biomedical photoacoustic measurements in time and frequency domains. Rev Sci Instrum 2010;81:124901.

[10] Petschke A, La Riviere PJ. Comparison of intensity-modulated continuous-wave lasers with a chirped modulation frequency to pulsed lasers for photoacoustic imaging applications. Biomed Opt Express 2010;1:1188–95.

[11] Lashkari B, Mandelis A. Comparison between pulsed laser and frequency-domain photoacoustic modalities: signal-to-noise ratio, contrast, resolution, and maximum depth detectivity. Rev Sci Instrum 2011;82:094903.

[12] Dovlo E, Lashkari B, Mandelis A, Shi W, Liu F. Photoacoustic radar phase-filtered special resolution and co-registered ultrasound image enhancement for tumor detection. Biomed Opt Express 2015;6:1003–9.

[13] Schleichert U, Paul M, Hoffmann B, Langenberg KJ, Arnold W. Theoretical and experimental investigation of broadband thermoelastically generated ultrasonic pulses. In: Hess P, Pelzl J, editors. Photoacoustic and photothermal phenomena. Berlin, Heidelberg: Springer; 1988. p. 284–7.

[14] White RM. Generation of elastic waves by transient surface heating. J Appl Phys 1963;34:3559.

[15] Achenbach JD. Wave propagation in elastic solids. Amsterdam: North-Holland; 1973. p. 6. chap. 2.

[16] Huan H, Mandelis A, Lashkari B, Liu L. Frequency-domain laser ultrasound (FDLU) non-destructive evaluation of stress/strain behavior in an aluminum alloy. Int J Thermophys 2017;38(4):62.

[17] Wu Y, Shi D, He Y. Study of the directivity of laser generated ultrasound in solids. J Appl Phys 1998;83:1207.

[18] Shampine LF. Vectorized adaptive quadrature in MATLAB. J Comput Appl Math 2008;211:131–40.

[19] Mandelis A. Frequency modulated (FM) time delay photoacoustic and photothermal wave spectroscopies. Technique, instrumentation, and detection. Part I: Theoretical. Rev Sci Instrum 1985;57(4):617–21.

[20] Lashkari B. Photoacoustic imaging using chirp technique: comparison with pulsed laser photoacoustics PhD Dissertation University of Toronto; 2011 p. 42–6.

[21] Gilat A, Clifton RJ. Pressure-shear waves in 6061-T6 aluminum and alpha-titanium. J Mech Phys Solid 1985;33(3):263–84.

[22] ANSI 304 stainless steel data at: https://www.makeitfrom.com/material-properties/6061-T6-Aluminum.

[23] Morath C, Stoner RJ. Method and apparatus for increasing signal to noise ratio in a photoacoustic film thickness measurement system. 2006:US7050178.

[24] Shin HJ, Song SJ. Time-frequency analysis of Lamb waves for distance and thickness measurement. AIP Conf. Proc. 2001;557:149.

[25] ANSI 304 stainless steel data at: https://www.makeitfrom.com/material-properties/AISI-304-1.4301-S30400-Stainless-Steel.